

Three-dimensional analysis of intermediate filament networks using SEM-tomography

Sebastian Lück^{1*} Michaela Sailer^{2*} Volker Schmidt¹ Paul Walther²

September 11, 2009

Abstract

We identified tomographic reconstruction of a scanning electron microscopy tilt series recording the secondary electron signal as a well-suited method to generate high contrast 3D data of intermediate filament (IF) networks in pancreatic cancer cells. Although the tilt series does not strictly conform to the projection requirement of tomographic reconstruction, this approach is possible due to specific properties of the detergent-extracted samples. We introduce an algorithm to extract the graph structure of the IF networks from the tomograms based on image analysis tools. This allows a high-resolution analysis of network morphology, which is known to control the mechanical response of the cells to large-scale deformations. Statistical analysis of the extracted network graphs is used to investigate principles of structural network organisation which can be linked to the regulation of cell elasticity.

Keywords : CYTOSKELETON, INTERMEDIATE FILAMENTS, SEM-TOMOGRAPHY, NETWORK MORPHOLOGY

1 Introduction

The cytoskeleton of eucaryotic cells is composed of three biopolymer systems: the network of actin filaments, the system of microtubuli and the network of intermediate filaments (IF). This study focusses on the network of IFs, which have a diameter of between 10 and 12 nanometres(*nm*) (Coulombe & Omary, 2002) and are formed by a heterogenous group of proteins with a tissue specific expression. In epithelial cells and their tumors like the human pancreatic cancer cells considered in this study, IFs mainly consist of keratins K8 and K18 (Fuchs, 1994).

IFs possess a particularly high extensibility and resistance to breakage (Herrmann et al., 2007 and references therein). Therefore, they govern the elastic properties of a cell when it is exposed to deformations of large scale and override the impact of the actin network (Beil et al., 2003; Suresh et al., 2005). IF as well as actin networks are formed of semiflexible polymers. It is known from numerical simulations and experimental studies that networks composed of semiflexible polymers exhibit a much stronger interplay between network morphology and elasticity than observed in flexible polymer networks (Heussinger & Frey, 2006 and 2007;

*These authors contributed equally.

†corresponding author

¹Institute of Stochastics, Ulm Germany University, D-89069 Ulm, Germany

²Electron microscopy facility, Ulm University, D-89069 Ulm

Gardel et al., 2004). It is therefore of interest to develop methods for the visualization and image analysis of IF networks, which allow for detailed assessment of morphological network characteristics. In previous studies this was done based on 2D scanning electron microscopy (SEM) (Beil et al., 2005 and 2006). This is an appropriate technique for networks observed in the cell periphery, which exhibit an almost planar structure. Nevertheless, in other cellular compartments IF networks can possess a genuinely 3D architecture. Numerical simulations revealed that the mechanical behavior of 3D biophysical networks can be intrinsically tied to morphological characteristics of 3D nature (Huisman et al., 2007). These characteristics comprise connectivity and segment length, which for non-planar networks can only be adequately assessed from 3D image data. In this study we introduce a method that allows to monitor the 3D structure of IF networks and we statistically investigate the interplay of certain mechanically relevant network characteristics in pancreatic cancer cells.

Since the diameter of IFs and interfilament distances are smaller than the diffraction limit of light microscopy, an analysis of network morphology at the level of single filaments and their cross-links cannot be achieved by fluorescence imaging of living cells (Windoffer et al., 2004; Wöll et al., 2007). A widely applied electron microscopical method to visualize cytoskeletal filament networks such as IFs, is detergent extraction of the cells, followed by chemical fixation and critical point drying. The samples are then coated with a thin layer of heavy metal or carbon and can be visualized either in the SEM or, after replication, in the transmission electron microscope (TEM; e.g. Svitkina & Borisy, 1999).

The natural approach to obtain 3D image data of IF networks would be tomographic reconstruction of a TEM or scanning TEM (STEM) tilt series. Transmission images are appropriate for tomography since they are projections of the specimen as required by all tomographic reconstruction algorithms. However, the volume-dependent transmission electron signal yields rather low contrast of the thin filaments in comparison to the strong signal of non-IF cytoplasmic components that are not completely removed during extraction. We therefore suggest an approach using the surface-dependent secondary electron signal, which is relatively strong from the filaments. Due to the extraction protocol single filaments are visible on secondary electron images under most tilt angles. Thus, these tilt images can be viewed as a good approximations for projections of a modified density, which highlight the filamentous structures. Reconstructions of secondary electron tilt series yielded substantially increased filament contrast in comparison to TEM and STEM.

Although scanning electron microscopy also comprises techniques which do not use secondary electrons such as STEM, for the ease of wording, we will sometimes replace the term ‘secondary electron’ by the simple prefix ‘SEM’. Thus, in this work, whenever the term ‘SEM’ is used, we refer to secondary electron data such as single tilt images or tomograms.

Analysis of network morphology requires the extraction of the network connectivity graph from the tomograms. For this purpose we combined standard techniques from image analysis, namely thresholding and skeletonization, with a specifically designed algorithm that reduces artefacts arising from errors in continuity tracking and tomographic reconstruction of secondary electron tilt series. Based on this data, we statistically investigated the morphology in different samples of IF networks. This statistical analysis revealed principles of network organization, which can be linked to the regulation of cell elasticity.

2 Material and Methods

2.1 Cell culture

Panc1 human pancreatic cancer cells (American Type Culture Collection, Manassas, VA, USA) were grown as a monolayer on glow discharged sapphire discs coated with carbon as described by Buser et al. (2007).

2.2 Cell preparation

The preparation of cells to visualize the keratin network by high-resolution SEM by a prefixation extraction method (Ris, 1985) was partially based on the protocol of Svitkina & Borisy (1998). After washing with phosphate-buffered saline (PBS; pH 7.3), the cells were extracted for 25 minutes at around 8°C with 1% Triton-X 100 (in PBS). Cells were washed again with PBS and fixed with 2.5% glutar aldehyde (in PBS, with distilled water and 1% saccharose) for 1 hour at room temperature. After washing with PBS, the cells were contrasted with OsO₄ (2% in PBS) for 1 hour at room temperature. After another washing step with PBS, the samples were gradually dehydrated in 30%, 50%, 70%, 90%, and 100% propanol (for 5 minutes at each step). Then the cells were critical-point dried using carbon dioxide as translation medium (Critical Point Dryer CPD 030, BalTec, Principality of Liechtenstein). Finally, the samples were perpendicularly coated with a thin layer of carbon by electron beam evaporation (5nm; BalTec Baf 300).

2.3 Electron microscopy

To analyze the filamentous structure of the keratin network, the grids were imaged with a Hitachi S-5200 in-lens SEM (Tokyo, Japan) at an accelerating voltage of 5 kilovolts (*kV*) using the secondary electron signal. Since the stage of the SEM allows only a maximal tilt of 40°, we mounted the samples on a pretilted (35°) specimen holder. After having recorded the series from +60° to 0°, the sample was rotated by 180° and remounted in order to record the second series from 0° to -60°. (At tilt angles above 60° contrast became very poor most likely due to self-shadowing effects.) Tilt series were recorded with 2° step size at a magnification of 50,000. In total 11 tomograms were recorded. Tomograms were reconstructed by weighted backprojection (WBP) with the IMOD software (Kremer et al., 1996) (Fig. 5 (a) and (b)).

3 Image segmentation

3.1 Image processing in Avizo

As a first step towards extracting the graph structure of the IF network from the tomograms, image filters provided by the Avizo software package (Mercury computer systems, 2008) were applied. Noise was reduced by an edge-preserving smoothing algorithm which consists of Gaussian filtering followed by an anisotropic diffusion, which guarantees that diffusion stops at edges within the image. Afterwards the image was binarised by thresholding and subsequent elimination of small islands in the foreground phase as well as some smoothing of the boundary (Fig. 5(d) and 1(a)). Since due to shadowing effects the secondary electron signal from filaments in lower layers of the cell tends to be weaker than the signal from

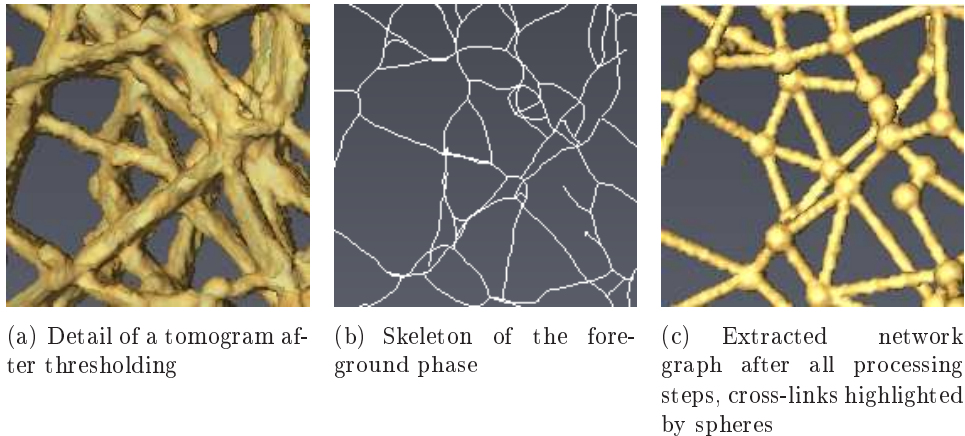


Figure 1: Extraction of the graph structure from a detail section of a secondary electron tomogram

upper parts of the network, thresholding was done semiautomatically, i.e. thresholds were adapted manually to the brightness level of the different network components, which were then automatically identified based on connectivity. In a next step a homotopic, i.e. connectivity-preserving, skeleton of the filamentous phase was computed by the skeletonisation package of Avizo (Fourard et al., 2006) (Fig. 1(b)). The skeletonisation result was reduced to its graph structure and exported as vector data, where the filament trajectories were represented as polygon tracks. The subsequent steps of image processing were based upon the graph of the skeletonisation result obtained in this way and implemented in the Geostoch software library (Mayer et al., 2004). An example of a final segmentation result can be seen in Fig. 1(c). Several corrections were applied to the graph structure obtained from the Avizo software in order to compensate for artefacts resulting from binarisation, skeletonisation or missing information which would have been needed for unbiased tomographic reconstruction.

3.2 Removal of loops and linearisation of filaments

The images of the tilt series suggested that loops, i.e. filaments starting and ending at the same point had to be regarded as artefacts. Therefore, all loops were removed from the network graph. Moreover, since filaments exhibited only negligible curvature, network vertices of degree 2, i.e. nodes joining exactly two edges, were removed from the graph unless the corresponding line segments enclosed an angle of less than 270° . Whenever a vertex of degree 2 was removed, the corresponding connection was replaced by a single line segment.

3.3 Optimisation of segment positions

Although the filaments on the tilt series images exhibited hardly any curvature, the line segments of the graph representing the filaments still had to be regarded as linear approximations of the actual filament shapes. Since they were constructed as straight connections between filament linking points their position did possibly not optimally resemble the filament trajectories in the threshold images. An algorithm was designed in order to improve the position of all line segments within the filamentous phase of the tomograms. Details are given in Appendix A. The algorithm takes particular care to center the extracted network segments in z -direction within the filamentous phase since binarised tomograms exhibited some filament

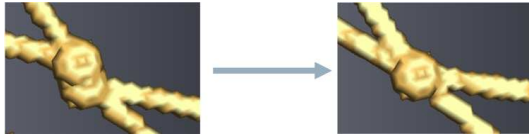


Figure 2: Merging of closely located cross-links

profiles whose height exceeded their width by up to factor 3, although in reality the profile of IFs is circular. This inaccuracy of the resolution in z-direction is a consequence of the limited tilt range in electron tomography (the missing wedge problem see e.g. Bartesaghi et al. (2008) and Midgley & Dunin-Borkowski (2009)) and a certain oversegmentation in upper network layers, which could not be avoided if threshold values were used which still allowed for identification of lower network components exhibiting reduced contrast. The optimisation algorithm for segment positioning was repeated after each step of graph modification described below.

3.4 Merging of closely located cross-links

Since some filaments are entangled in such a way that they enclosed small angles, filament links located very closely to each other were regarded as artefacts. Therefore, as suggested in Beil et al. (2005), such pairs of filament links were merged into a single one located in their center of gravity (Fig. 2). Taking into account that after carbon coating filaments had a diameter between $20nm$ and $25nm$ merging was performed for network nodes of a distance less than $d = 36nm$ apart in ascending sequence, i.e. link pairs of smaller distance were merged first. Afterwards segment positions were optimized as described in Section 3.3.

3.5 Dead ends

In SEM images of IF networks one hardly observes filament ends which are not connected to other network components. In spite of this, in the network graphs extracted from the SEM tomograms such dead ends occurred. A certain fraction of these were well-known artefacts of the skeletonization algorithm (Soille, 1999). However, some dead ends also resulted from principle limitations of the technique of SEM tomography. In contrast to TEM, the SEM tilt series does not consist of projections of the specimen but measures the surface-dependent secondary electron signal. As a consequence, due to shadowing effects in areas of dense network structure lower filament layers were partially not visible or only at less contrast. Therefore, some trajectories of lower level filaments were truncated in the binarised tomograms (Fig. 3). These artefacts were reduced by an algorithm which establishes extrapolations of dead ends within the network graph and checks them for plausibility. A detailed description of the algorithm can be found in Appendix B. Dead ends which did not have a plausible extrapolation as defined by this algorithm were regarded as skeletonisation artefacts and removed from the network graph unless they were close to the boundary of the observation window.

4 Statistical analysis of network morphology

By means of 3D numerical finite element simulations of semiflexible polymer networks, correlations between network stiffness and the three morphological characteristics network density,

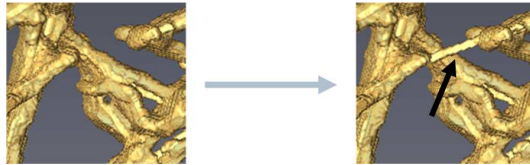


Figure 3: Extrapolation of a dead end

defined in terms of filamentous polymer concentration in the system, average segment length and connectivity have been demonstrated (Huisman et al., 2007). These results motivated our choice of network characteristics for the analysis of IF networks in Section 5. Their definitions will now be made precise. Since after preparation of the cells and tomographic reconstruction the actual 3D volume of the cellular compartments is hard to be estimated, we defined network density as the total network length per base area. It should be emphasized that this definition of network density purely focusses on the amount of polymers forming the network and not on network architecture. Since the amount of filamentous polymers is controlled by synthesis and phosphorylation status of IF proteins (Coulombe & Omary, 2002), network density defined in this way can be directly linked to biological processes. Other measures of density such as cross-link density are not only tied to the amount of polymers but to structural characteristics of network architecture, which in this study are assessed separately by mean segment length and connectivity.

If mean segment length is measured as the total network length divided by the number of segments, one obtains a biased estimator. This is due to the fact that the length of filaments protruding the observation window is underestimated. In order to avoid these edge effects the mean was only taken with respect to segments whose center was located in a smaller sampling window. The base of this sampling window was chosen as the central $1.84 \times 1.2 \mu\text{m}^2$ of the observation window, its height was not restricted since filaments did not protrude the observation window in the third dimension.

Network connectivity was measured by considering the mean vertex degree of the network, where the degree of a vertex (i.e. a cross-link in the network) is defined as the number of segments emanating from it.

Network density, mean segment length and mean vertex degree were computed for 11 tomograms of IF networks in pancreatic cancer cells. Our statistical analysis primarily focusses on the interplay of these characteristics, namely their mutual correlations. These can be exploited to infer the relation of different principles applied by the cells in order to vary network architecture, and thus change their elasticity. When working with relatively small sample sizes, estimated values for correlation coefficients of two random variables can be misleading due to stochastic variability. Meaningful results concerning the correlation of different morphological network characteristics can however be obtained by testing if the measure of correlation significantly differs from zero. Standard tests for correlation exploit the distribution of Pearson's correlation coefficient. However, the latter depends on the bivariate distribution of the sample vectors to be investigated, which at small sample sizes can hardly be inferred. Naturally, for small sample sizes also asymptotic tests are inappropriate. As a remedy, instead of Pearson's correlation coefficient we considered Spearman's rank order correlation coefficient ρ_S and Kendall's coefficient of concordance τ (for a definition see e.g. Sheskin, 2000). Under the assumption of uncorrelated, identically and continuously distributed sample vectors $(X_1, Y_1), \dots, (X_n, Y_n)$ the distributions of Spearman's ρ_S and Kendall's τ do not depend on the distribution of the sample vectors. Therefore, for both of these measures of correlation nonparametric statistical tests are available, which can already be applied at small sample sizes (Sheskin, 2000). The detailed construction of the

tests can be found in Hollander & Wolfe (1973). The tests can be used to detect dependencies of the following type:

- (a) There is a tendency of the larger values of X_1, \dots, X_n to be paired with the larger values of Y_1, \dots, Y_n .
- (b) There is a tendency of the larger values of X_1, \dots, X_n to be paired with the smaller values of Y_1, \dots, Y_n .

The null hypothesis of the tests is ‘no correlation between the two samples’, i.e. $H_0 : \rho_S = 0$ or $H_0 : \tau = 0$, respectively. H_0 can be tested against the one-sided alternative of positive correlation (i.e. (a)), against the alternative of negative correlation (i.e. (b)) or against the two-sided alternative (i.e. (a) or (b)).

5 Results

We investigated several preparation and imaging protocols for preservation and recording of the 3D IF network. The first one was high-pressure freezing, freeze substitution, embedding and thin sectioning. We analyzed these samples with regular TEM, 300kV Scanning TEM (STEM) and 30kV STEM (Sailer et al., 2009). It turned out, however, that on these samples it was difficult to track the individual filaments in the very complex context of all the retained cellular structures of unextracted cells. We analyzed, therefore, intermediate filament networks from detergent-extracted cells. When imaging these samples with a 300kV STEM, the signal of the thin filaments was relatively poor, it could be increased by using a 30kV STEM, but still the signal of the filaments was insufficient compared to the strong signal of non-IF cytoplasmic components that were not completely removed during extraction (Fig. 4(a)). Therefore, we used the secondary electron signal, which is surface-dependent and relatively strong from thin filaments (Fig. 4(b)). As a consequence of detergent extraction even single filaments in some depth are clearly visible under most tilt angles. Therefore, they are captured by tomographic reconstructions of secondary electron tilt series (Fig. 5(c)). The datasets were recorded by tilting the sample similar to TEM-tomography. The tilt series was then back-projected into a three-dimensional model.

In our setting the input signal of the reconstruction algorithm was not a projection of the specimen as required by the mathematical theory of WBP, but a surface dependent signal (Joy & Pawley, 1992). Simulated signals were used to clarify the impact of the violated projection requirement on the reconstruction of single filaments. In the parallel beam geometry of single-axis electron tomography the reconstruction of a 3D volume is done by separate reconstruction of parallel 2D slices from their 1D projections. In most orientations of a filament with respect to the tilt axis its intersection with a 2D slice of the considered volume is an ellipse. Therefore, we simulated the surface dependent and the projection signal of a 2D circle and compared the corresponding WBP reconstructions. The diameter was chosen as 11 pixel lengths, which is comparable to the diameter of an IF at the resolution used for this study. The surface dependent signal at a pixel of a tilt image was modeled to be proportional to the boundary length hit by a beam whose width was chosen as one pixel length. The value of a simulated projection at a particular pixel was chosen to be proportional to the area within the circle that got projected onto the pixel. Both signals were normalized in order to obtain the same total signal strength for projections and surface rendering.

Fig. 6 illustrates that the WBP reconstruction based on a surface dependent signal (Fig. 6(b)) does not differ substantially from the reconstruction obtained from projection data (Fig. 6(a)).

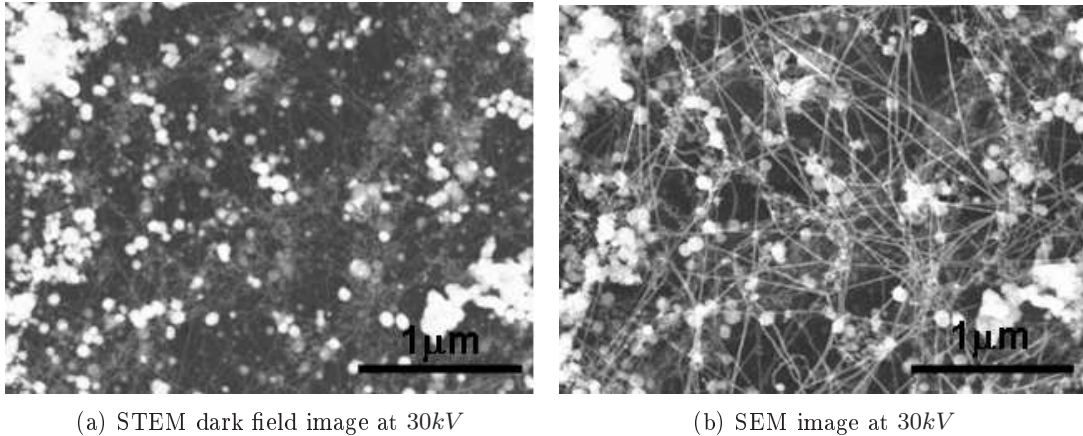


Figure 4: STEM dark field and SEM secondary electron images taken from the same intracellular location at 0° tilt. STEM images provided a rather low signal of IFs in comparison to the strong signal of non-IF cytoplasmic leftovers after extraction of the cells. Secondary electron imaging enhanced the signal of IFs.

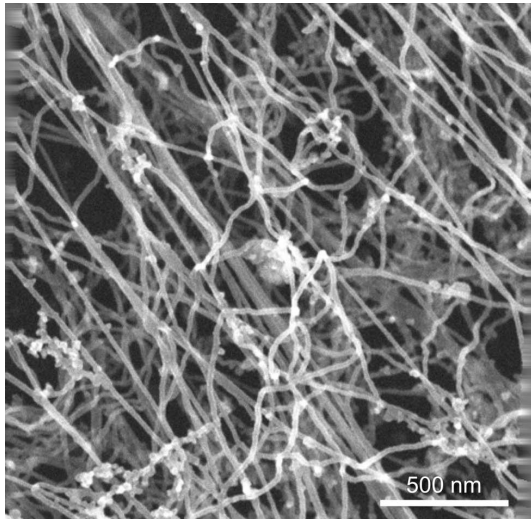
The main difference is a slightly more faded interior of the circle in the reconstruction based on the surface signal in comparison to the one obtained from projections. In backprojections of experimental SEM tilt series the fading in the interior of the filaments was less noticeable than for the simulated data. This is plausible since in the WBP reconstruction of an imperfectly aligned tilt series the relatively high density, which under ideal alignment is found along the boundary of the reconstructed object, is spread over a larger area. This is a consequence of the superposition of backprojections under different tilt angles in the WBP algorithm (Buzug, 2008).

In order to monitor the impact of shadowing effects, WBP reconstructions were computed from the simulated SEM tilt series of the circle where the signal was set to zero over a variety of tilt ranges. Fig. 7 (d)-(e) illustrate the effect of shadowing for the central part of the tilt range, where the information of the central 40° , 60° , and 80° is missing, respectively. The missing information results in decreased contrast. Furthermore, the reconstruction of the circle approaches a square. Fig. 7 (a)-(c) depict the most frequent shadowing scenario occurring for filaments in deeper network layers of our experimental data, namely shadowing at high tilt angles. In this setting the reconstruction of the circle exhibited an oval shape at decreased contrast to the background. The loss in contrast was more extreme than observed in the experimental data, where WBPs were computed from tilt series with small imperfections in alignment. As discussed above, density was therefore more evenly spread over the filament profiles than on a WBP under ideal alignment such that contrast was increased.

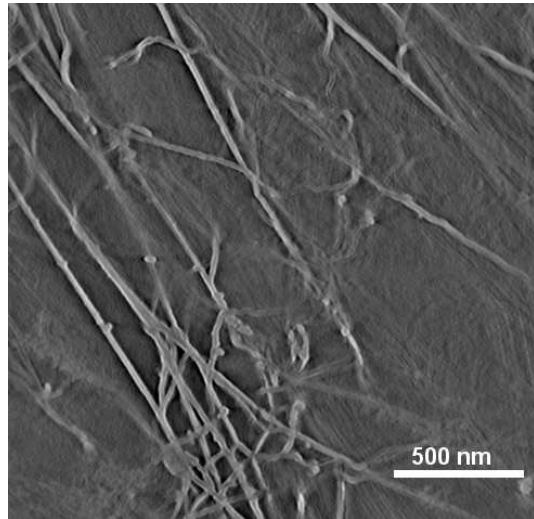
Morphological network characteristics were computed for 11 tomograms, where sampling regions were chosen at random throughout the entire cytoplasm. Network densities varied between $0.0082nm^{-1}$ and $0.0133nm^{-1}$ with mean $0.01nm^{-1}$ and standard deviation $0.0019nm^{-1}$ (Fig. 8(a)). The spread between minimal and maximal network density observed was thus equivalent to 51% of the mean value of the network densities.

The mean segment length in the tomograms varied between $93nm$ and $137nm$, its mean and standard deviation being $111nm$ and $13.6nm$, respectively. The spread between maximum and minimum mean segment length corresponds to 40% of the average mean segment length (Fig. 8(b)).

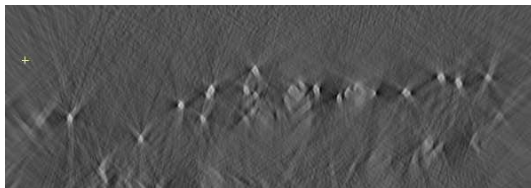
Measurements of the mean vertex degree indicated substantial variability of network connectivity. Values varied between 3.5 and 4.2 with a standard deviation of 0.23. This spread



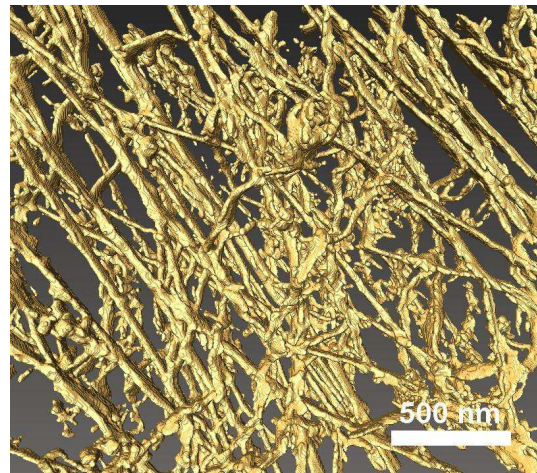
(a) SEM image at 0° tilt



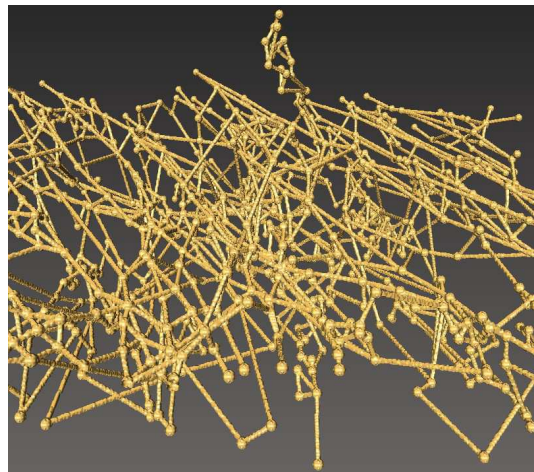
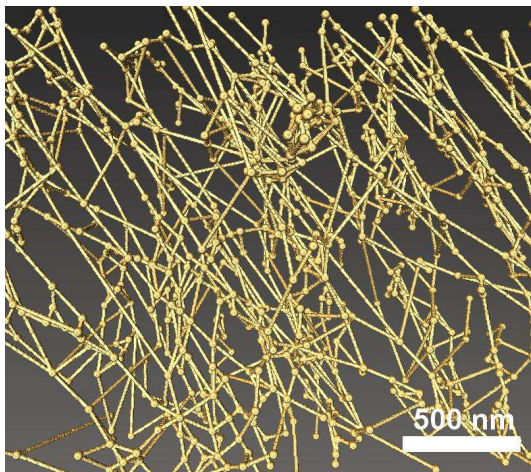
(b) Horizontal cut through an SEM tomogram



(c) Vertical cut through an SEM tomogram

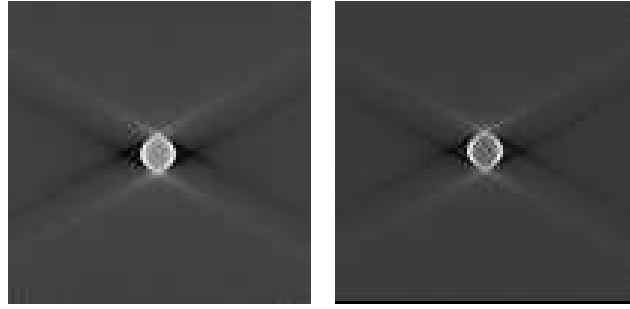


(d) Tomogram after binarisation (top view)



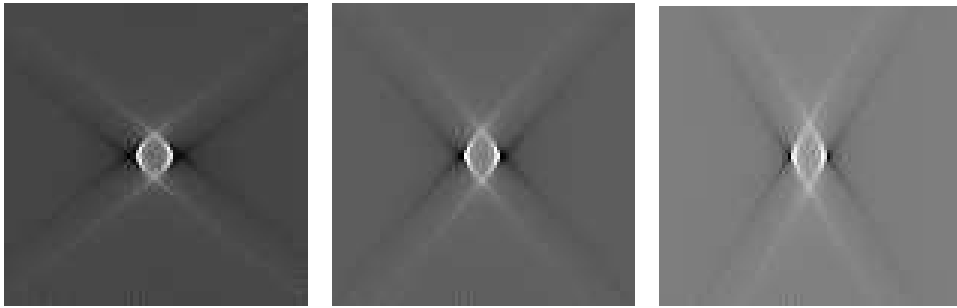
(e) Network graph extracted from the tomogram, top view (left), rotated by 40° around central axis (right)

Figure 5: IF network in a detergent extracted Panc1 cell visualized at a magnification of 50,000. Filaments in some depth are clearly visible at good contrast in the secondary electron tomogram. The graph extracted from the tomogram exhibits a genuinely 3D structure.

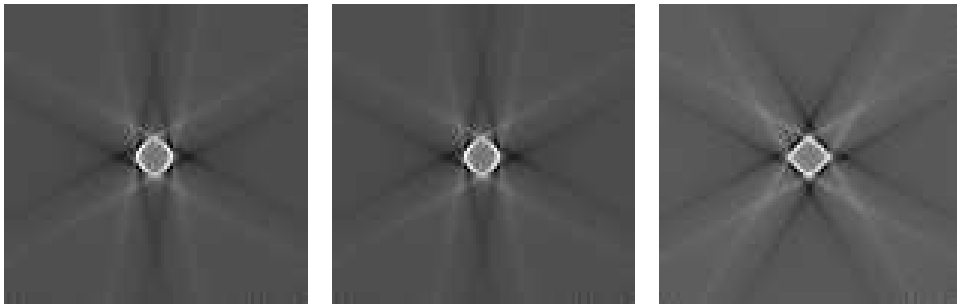


(a) WBP from simulated TEM signal (b) WBP from simulated secondary electron signal

Figure 6: WBP reconstructions of a circle (diameter 11 pixel lengths) from simulated projections (corresponding to TEM) and from a simulated surface dependent signal (corresponding to the secondary electron signal of SEM). The tilt range was chosen from -60° to $+60^\circ$ at an increment of 2° .



(a) Shadowing for tilt angles in $(-60^\circ, -50^\circ)$ and $(50^\circ, 60^\circ)$ (b) Shadowing for tilt angles in $(-60^\circ, -40^\circ)$ and $(40^\circ, 60^\circ)$ (c) Shadowing for tilt angles in $(-60^\circ, -30^\circ)$ and $(30^\circ, 60^\circ)$



(d) Shadowing for tilt angles in $(-20^\circ, 20^\circ)$ (e) Shadowing for tilt angles in $(-30^\circ, 30^\circ)$ (f) Shadowing for tilt angles in $(-40^\circ, 40^\circ)$

Figure 7: WBP reconstructions of a circle (diameter 11 pixel lengths) from a simulated secondary electron signal with shadowing effects. The tilt range was chosen from -60° to $+60^\circ$ at an increment of 2° .

corresponds to 20% of the average mean vertex degree with respect to all tomograms, which was 3.7. Maximum connectivity was measured for tomogram 3, which exhibited increased relative frequencies of vertices of degree 4 and even higher (Fig. 9(a)). Vertex degrees above 4 were observed if several IFs were linked by microgel structures (Fig. 10). Degree distributions with pronounced increases in relative frequencies of higher vertex degrees could also be observed in tomograms 4, 10 and 11. On the other hand, tomograms with extremely low connectivity such as samples 1, 2 exhibited a high frequency of vertices of degree 3.

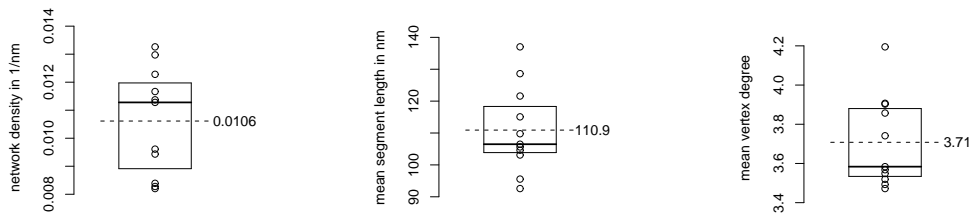
Since connectivity was assessed by vertex degrees it was important to monitor if the results were distorted by the merging parameter d in the segmentation algorithm, which ensures that network vertices of less than a distance d apart are replaced by a single cross-link (Section 3.4). Fig. 11 shows that the mean vertex degree depended on the merging parameter. However, ranking of the different tomograms with respect to the mean vertex degree was rather stable. As a consequence, the test results for the rank-based correlation coefficients ρ_S and τ discussed below were hardly affected by the merging parameter. For these investigations d was not chosen smaller than $20nm$, since this would be less than the filament diameter after carbon coating and thus, shorter network segments can clearly be regarded as segmentation artefacts.

In order to assess whether changes of network density, mean segment length, and connectivity exhibit interdependencies, two statistical tests were performed for each pair of characteristics. The first one tested the null hypothesis that Spearman's rank-order correlation coefficient ρ_S was equal to 0 whereas the second one tested the analogous hypothesis for Kendall's τ . In both tests the alternative hypothesis was chosen as two-sided, i.e., any kind of correlation no matter if positive or negative leads to a rejection. As also suggested by the scatterplot in Fig. 12(a) the hypothesis that there is no significant correlation of network density and mean segment length is not rejected for Spearman's ρ_S ($p = 0.99$) and for Kendall's τ ($p = 1.0$). The tests also did not reject the hypothesis of uncorrelated changes of network density and mean vertex degree (Tab. 5.1, see also Fig. 12(b)). At the level of significance $\alpha = 0.1$ variations of the merging parameter d did not change test results (all p-values were above 0.29). Thus, independently of d the correlation coefficients did not significantly differ from 0.

Tests however indicated a significant negative correlation between mean segment length and mean vertex degree (Fig. 12(c)). More precisely, the null hypothesis of correlation coefficients being equal to zero was rejected at the 10%-level although not at the 5%-level (Tab. 5.1). The tests for correlation of mean segment length and mean vertex degree were also applied in their one-tailed version for negative correlation, i.e., H_0 was rejected if and only if the correlation coefficient (which was either ρ_S or τ) was less than its α quantile. In that case H_0 was even rejected at the 5% level ($p = 0.026$ and $p = 0.043$ for ρ_S and τ , respectively). At the 10% level, significant correlation was found for all merging distances $d \geq 28nm$. For $d = 24$, p-values increased to 0.16 for ρ_S and to 0.1 for τ . A merging distance of $d = 20$ did not exhibit significant correlation of mean segment length and mean vertex degree. Since we identified $d = 36nm$ as a reasonable merging parameter to suppress artefact formation, one can conclude that test results behaved stable for suitable choices of d .

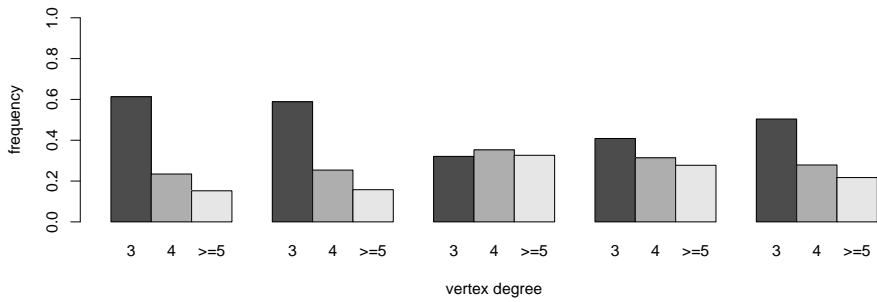
6 Discussion

The architecture of the IF network plays a pivotal role for cell migration by regulating cell viscoelasticity (Beil et al., 2003). In networks formed by semiflexible polymers such as IF even small alterations of network architecture can significantly change the elasticity of the network and, hence, the mechanical properties of cellular compartments (Morse, 1998; Gardel

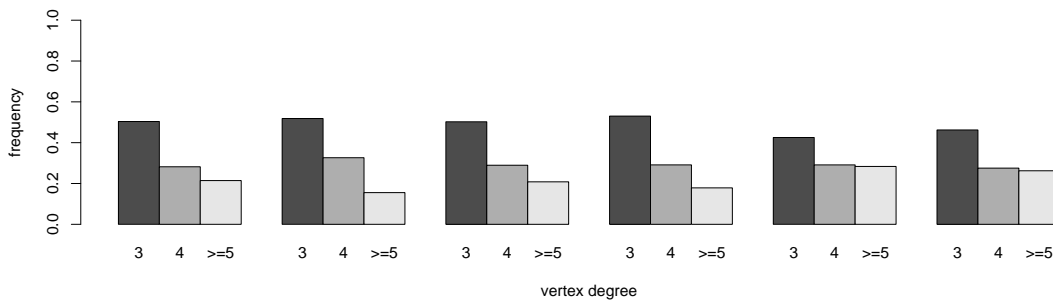


(a) Network density (b) Mean segment length (c) Mean vertex degree

Figure 8: Boxplots of network density, mean segment length and mean vertex degree that were computed for 11 tomograms. Bold lines depict medians, whereas dashed lines indicate the sample means, whose values can be found to the left of the boxes.

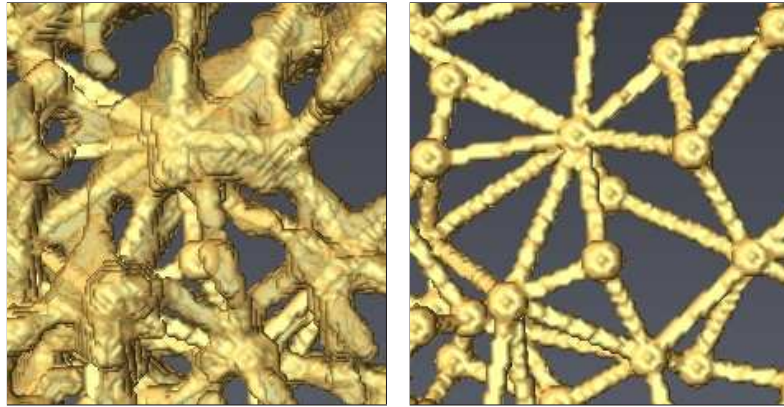


(a) Tomograms 1 – 5 (from left to right)



(b) Tomograms 6 – 11 (from left to right)

Figure 9: Fractions of vertices with degree 3, 4 and ≥ 5 (with respect to all vertices of degree at least 3)



(a) Section of a thresholded tomogram (b) Extracted graph structure

Figure 10: Filaments connected by a microgel structure

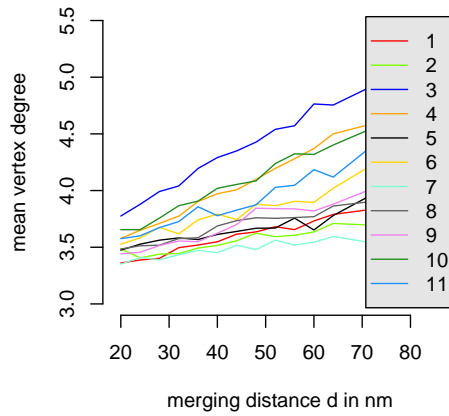
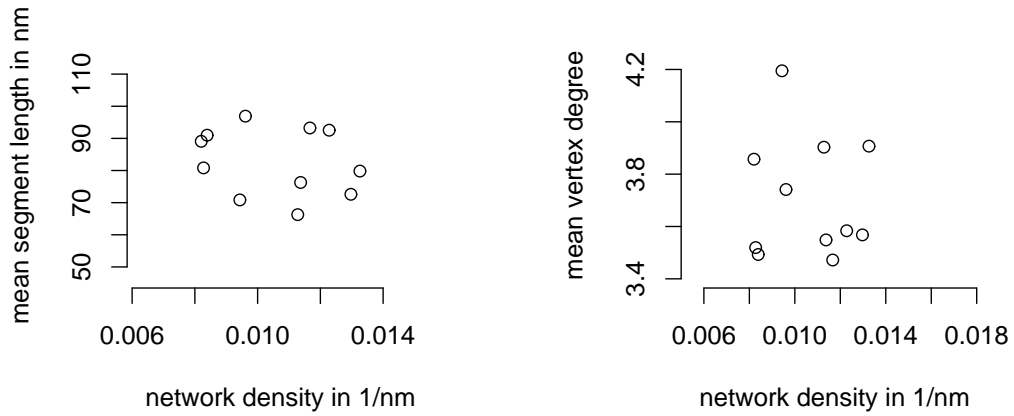


Figure 11: Mean vertex degree as a function of the merging distance d in the segmentation algorithm

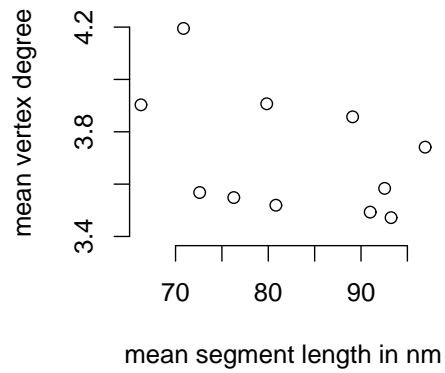
p-values	mean segment length	mean vertex degree
network density	0.99	0.85
mean segment length	1.0	1.0
		0.05
		0.09

Table 5.1: Test results for the hypothesis of uncorrelated changes in the depicted pairs of network characteristics. The table contains p-values of tests for $H_0 : \rho_S = 0$ (upper values) and $H_0 : \tau = 0$ (lower values) against the two-sided alternative. The hypothesis of uncorrelated variation of two characteristics is rejected at a level of significance α , once the corresponding p-value does not exceed α . Hence both tests detect a significant correlation of mean segment length and mean vertex degree at the level of $\alpha = 0.1$, whereas there is no significant correlation between network density and each of the other two characteristics.



(a) Network density vs. mean segment length

(b) Network density vs. mean vertex degree



(c) Mean segment length vs. mean vertex degree

Figure 12: Scatterplots displaying the correlation between network characteristics

et al., 2004). Numerical studies and physical models for networks in 2D can provide valuable information on the relation between 2D network morphology and the elastic shear modulus of the networks (Head et al., 2003; Heussinger & Frey, 2006 and 2007; Fleischer et al., 2007). Nevertheless, although IF networks in the cell periphery often exhibit an almost planar structure (Beil et al. 2005), in less flat cellular compartments the IF cytoskeleton can clearly form a genuinely 3D biophysical network (Fig. 5 (c)), which in comparison to the 2D case possesses additional degrees of freedom with respect to morphology and mechanical behavior (Huisman et al., 2007). The methodology of this study allows one to investigate IF network morphology in 3D at high resolution. This way, we were able to compute network characteristics from a tomographic data set, which for non-planar networks can only be assessed from 3D image data. These comprise connectivity and the length of network segments, which in a correlative numerical study have been identified as relevant parameters for the elasticity of semiflexible polymer networks (Huisman et al., 2007).

There exist a number of papers discussing detergent extraction for TEM replicas (e.g. Svitkina, 2007). These datasets still represent the generally accepted standard on which the textbook models of cytoskeleton structures as e.g. in Alberts et al. (2008) are based. For actin networks artefact formation caused by detergent extraction, such as filament branching and visibility of the helical arrangement of G-actin subunits has been discussed in Resch et al. (2002) and Walther (2008). Therefore, alternative methods, such as cryo-TEM were introduced. In pioneering work by Medalia et al. (2002) the actin filament network in a very thin protrusion of the slime mould dictyostelium was tomographically visualized by cryo-TEM. This method is currently restricted to very thin samples; compartments of Panc 1 cells with non-planar IF networks would be too thick. In future work, we plan to combine detergent extraction with freeze drying methods (Walther, 2008) in order to reduce the danger of artefact formation. Data obtained by detergent extraction and critical point drying needs to be interpreted with care. However, first experiments with freeze-dried samples do not show obvious structural differences with respect to network structure.

A notable phenomenon on our images is that filaments appear considerably thicker (20 to 25nm) than described in the literature (10 to 12nm) (Coulombe & Omary, 2002). This could be due to a number of factors: The samples are fixed with glutaraldehyde and osmium tetroxide. Parts of this fixatives could attach onto the filaments and increase the measured thickness. Carbon coating was done perpendicular to the sample, without rotation. The thickness of 5nm was measured by a quartz crystal thickness monitor, which is a flat object. If carbon coating would be purely geometrical, the 5nm would be added only at the top of the filaments and not influence the measured thickness, at least at 0° tilt angle. However, carbon is reflected during coating by the objects, so that it sticks to the filaments and increases the filament diameter by a not fully predictable amount. Finally, SEM imaging itself bears some error, since the electron probe is not infinitely small but has a certain diameter, and as in any kind of scanned imaging, the structure visible in the picture is a convolution of the sample and the imaging probe.

At first sight, tomogram generation based on an SEM tilt series may appear counterintuitive, since the input data is surface dependent and thus violates the projection requirement of tomographic reconstruction. Nevertheless, the contrast in STEM projections of the keratin networks in detergent extracted cells turned out to be so low that continuity tracking of the filaments in the reconstructed tomograms was hardly possible. Since for this study detergent extracted cells were investigated, single filaments were clearly visible at most tilt angles and could therefore be mapped by the surface dependent secondary electron signal yielding high contrast images. Thus, the single images of the SEM tilt series could be viewed as good approximations for projection images of a modified density distribution within the

observed volume. These modifications were such that filaments were highlighted and the grey level of non-IF cytoplasmic components which had not been removed during extraction was decreased. Shadowing effects as illustrated in Fig. 7 weakened contrast in lower levels of the tomograms and posed a certain difficulty for segmentation of the image in filamentous and background phase. This was therefore not done by a global thresholding procedure but semiautomatically by means of the Avizo software package, where thresholds were selected manually for different parts of the network that were then identified automatically based on connectivity. Imperfections of the segmentation resulting in dead ends within the network graph were additionally reduced by the extrapolation algorithm discussed in Section 3.5. For the extraction of the network graph from the thresholded tomogram it was also taken into account that the missing tilt wedge and shadowing effects lead to ovally stretched filament profiles in the binarized tomograms. This was compensated for by an algorithm centering the extracted line segments within the filamentous phase (Section 3.3). It should be emphasized that after semiautomatic binarisation of the tomograms into filamentous phase and background, network graphs were extracted by a fully automatic algorithm. This way potential bias introduced by manual segmentation was minimized.

The thickness of the networks investigated in this study was up to $550nm$, not taking into account single filaments protruding from the main network body. The method of SEM tomography for detergent extracted samples is not primarily limited by sample thickness but by network density. In our samples we could detect up to three filaments on top of each other. Nevertheless, for denser networks this may not be possible if shadowing of deeper network components leads to a more limited visibility during tilting. On the other hand, in less dense networks even more layers of filaments may be reliably reconstructed in the tomograms.

Analysis of the extracted network graphs revealed a substantial morphological variability of IF networks in cultured human pancreatic cancer cells. For our analysis we focused on morphological network characteristics that can influence the elastic modulus of semiflexible polymer networks (Huisman et al., 2007), namely network density, mean segment length and mean vertex degree. All of these are spatial averages of morphological characteristics and can thus be assumed to possess a stable behavior in the sense of ergodic limits. This makes them appropriate for statistical analysis at small sample sizes. Although the mean vertex degree depended on the merging parameter d of the segmentation algorithm, the latter being necessary to remove skeletonisation artefacts in image segmentation, highly and weakly connected networks could clearly be distinguished independently of the choice for d (Fig. 11).

Tomograms did not only exhibit substantial variations in network density but also in their mean segment length and connectivity as measured by the mean vertex degree. Tests for correlation between these characteristics revealed that there is no significant correlation between network density and mean vertex degree as well as between network density and mean segment length. On the other hand tests indicated negative correlation between mean segment length and mean vertex degree. Test results were similar when connectivity was assessed by an approach based on the relative length of minimum spanning trees (MST), that has been suggested in Beil et al. (2009). Since relative MST length and mean vertex degree were strongly correlated these results we not included in favour of a a more concise presentation. Our results suggest that the mechanically relevant structural characteristics connectivity and mean segment length cannot be viewed as a function of network density, which in our definition primarily measures the amount of filamentous protein in the network independently of network architecture. Thus, in addition to controlling the amount of IF protein forming the networks Panc1 cells apparently possess a second degree of freedom for adjusting network architecture in a way that influences the elastic modulus of the network. Since variations of mean segment length and connectivity do not require protein syntheses they are possibly

used as energy-efficient means for fine-tuning of mechanical properties. To the best of our knowledge there is currently no universal physical model that would allow for a computation of the elastic shear modulus of a 3D semiflexible polymer network based on morphological measurements and the material properties of single filaments. Since results of numerical correlation studies are dependent on specific material properties and the models used to generate virtual network data, they do not allow for immediate quantitative conclusions in other settings. They can however reveal principles defining the interplay between network morphology and mechanics, and hence yield substantial indications for mechanical effects caused by morphological variability. Independently from numerical simulations, experiments can be designed in order to combine micro- and nanomechanical measurements on fixed and living cells (Atakhorrami et al., 2006; Marti et al., 2008) with the method of SEM-tomography and image segmentation proposed in this study. This presents a promising experimental approach to correlate mechanical properties of the cells and 3D morphological characteristics of their IF network.

Acknowledgements. This work was funded by a grant from Deutsche Forschungsgemeinschaft (SFB 518 project B21). We would like to thank Michael Beil for helpful discussions and Guido Adler for constant support of the project.

References

- [1] Alberts, B., Johnson, A., Lewis, L., Raff, M., Roberts, K. & Walter, P. (2008) *Molecular Biology of the Cell*, 5th ed. Garland Publishing, New York.
- [2] Atakhorrami, M., Sulkowska, J.I., Addas, K.M., Koenderink, G.H., Tang, J.X., Levine, A.J., MacKintosh, F.C. & Schmidt, C.F. (2006) Correlated fluctuations of microparticles in viscoelastic solutions: Quantitative measurement of material properties by microrheology in the presence of optical traps. *Phys. Rev. E* **73**, 061501.
- [3] Bartesaghi, A., Sprechmann, P., Liu, J., Randall, G., Sapiro, G. & Subramaniam, S. (2008) Classification and 3D averaging with missing wedge correction in biological electron tomography. *J. Struct. Biol.* **162**(3), 436–450.
- [4] Beil, M., Micoulet, A., von Wichert, G., Paschke, S., Walther, P., Omary, M.B., Van Veldhoven, P.P., Gern, U., Wolff-Hieber, E., Eggermann, J., Waltenberger, J., Adler, G., Spatz, J. & Seufferlein, T. (2003) Sphingosylphosphorycholine regulates keratin network architecture and visco-elastic properties of human cancer cells. *Nat. Cell Biol.* **5**, 803–811.
- [5] Beil, M., Braxmeier, H., Fleischer, F., Schmidt, V. & Walther, P. (2005) Quantitative analysis of keratin filament networks in scanning electron microscopy images of cancer cells. *J. Microsc.* **220**, 84–95.
- [6] Beil, M., Eckel, S., Fleischer, F., Schmidt, H., Schmidt, V. & Walther, P. (2006) Fitting of random tessellation models to cytoskeleton network data. *J. Theor. Biol.* **241**, 62–72.
- [7] Beil, M., Lück, S., Fleischer, F., Portet, S., Arendt, W. & Schmidt, V. (2009) Simulating the formation of keratin filament networks by a piecewise-deterministic Markov process. *J. Theor. Biol.* **256**(4), 518–532.
- [8] Buser, C., Walther, P., Mertens, T. & Michel, D. (2007) Cytomegalovirus primary envelopment occurs at large infoldings of the inner nuclear membrane. *J. Virol.* **81**(6), 3042–3048.
- [9] Buzug T.M. (2008) *Computed Tomography*. Springer, Berlin.
- [10] Conover, W.J. (1971) *Practical Nonparametric Statistics*. J. Wiley & Sons, New York.
- [11] Coulombe, P.A. & Wong, P. (2002) ‘Hard’ and ‘soft’ principles defining the structure, function and regulation of keratin intermediate filaments. *Curr. Opin. Cell Biol.* **14**(1), 110–122.

- [12] Fleischer, F., Ananthakrishnan, R., Eckel, S., Schmidt, H., Käs, J., Svitkina, T., Schmidt, V. & Beil, M. (2007) Actin network architecture and elasticity in lamellipodia of melanoma cells. *New J. Phys.* **9**, 420.
- [13] Fourard, C., Malandain, G., Prohaska, S. & Westerhoff, M. (2006) Blockwise processing applied to brain microvascular network study. *IEEE Trans. Med. Im.* **25**, 1319–2006.
- [14] Fuchs, E. (1994) Intermediate filaments: Structure, dynamics, function and disease. *Annu. Rev. Biochem.* **63**, 345–382.
- [15] Gardel, M.L., Shin, J.H., MacKintosh, F.C., Mahadevan, L., Matsudaira, P. & Weitz, D.A. (2004) Elastic behavior of cross-linked and bundled actin networks. *Science* **304**, 1301–1305.
- [16] Head, D.A., Levine, A.J. & MacKintosh, F.C. (2003) Deformation of cross-linked semiflexible polymer networks. *Phys. Rev. Lett.* **91**, 108102.
- [17] Herrmann, H., Bär, H., Kreplak, L., Strelkov, S.V. & Aebi, U. (2007) Intermediate filaments: from cell architecture to nanomechanics. *Nat. Rev. Mol. Cell Biol.* **8**(7), 562–573.
- [18] Heussinger, C. & Frey, E. (2006) Stiff polymers, foams, and fiber networks. *Phys. Rev. Lett.* **96**, 017802.
- [19] Heussinger, C. & Frey, E. (2007) Role of architecture in the elastic response of semiflexible polymer and fiber networks. *Phys. Rev. E Stat. Nonlin. Soft. Matter. Phys.* **75**, 011917.
- [20] Hollander, M. & Wolfe, D.A. (1973) *Nonparametric Statistical Methods*. J. Wiley & Sons, New York.
- [21] Huisman, E.M., van Dillen, T.M., Onck, P.R. & Van der Giessen, E. (2007) Three-dimensional cross-linked F-actin networks: Relation between network architecture and mechanical behavior. *Phys. Rev. Lett.* **99**, 208103.
- [22] Joy, D.C. & Pawley, J.B. (1992) High-resolution scanning electron microscopy. *Ultramicroscopy* **47**(1-3), 80–100.
- [23] Kremer, J.R., Mastrorarde, D.N. & McIntosh, J.R. (1996) Computer visualization of three-dimensional image data using IMOD. *J. Struct. Biol.* **116**, 71–76.
- [24] Marti, O., Holzwarth, M. & Beil, M. (2008) Measuring the nanomechanical properties of cancer cells by digital pulsed force mode imaging. *Nanotechnology* **19**, 384015.
- [25] Mayer, J., Schmidt, V. & Schweiggert, F. (2004) A unified simulation framework for spatial stochastic models. *Simul. Model. Pract. Th.* **12**, 307–326.
- [26] Medalia, O., Weber I., Achilleas, S., Frangakis, D. N., Gerisch, G. & Baumeister, W. (2002) Macromolecular architecture in eukaryotic cells visualized by cryoelectron tomography. *Science* **298**, 1209–1213.
- [27] Midgley, P.A. & Dunin-Borkowski, R.E. (2009) Electron tomography and holography in materials science. *Nat. Mater.* **8**, 271–280.
- [28] Morse, D.C. (1998) Viscoelasticity of concentrated isotropic solutions of semiflexible polymers: 1. Model and stress tensors. *Macromolecules* **31**, 7030–7043.
- [29] Resch, G.P., Goldie, K.N., Krebs, A., Hoenger, A. & Small, J.V. (2002) Visualisation of the actin cytoskeleton by cryo-electron microscopy. *J. Cell Sci.* **115**, 1877–1882.
- [30] Ris, H. (1985) The cytoplasmic filament system in critical-point dried whole mounts and plastic embedded sections. *J. Cell Biol.* **100**, 1474–1478.
- [31] Sailer M., Lück, S., Schmidt, V., Beil, M., Adler, G., & Walther, P. (2009) Three-dimensional analysis of the intermediate filament network using SEM-tomography. *9th Multinational Conference on Microscopy*, Graz, Austria.
- [32] Sheskin, D.J. (2000) *Handbook of Parametric and Nonparametric Statistical Procedures, 2nd ed.* Chapman & Hall/CRC, New York.

- [33] Soille P. (1999) *Morphological Image Analysis, Principles and Applications*. Springer, Berlin.
- [34] Suresh, S., Spatz, J., Mills, J.P., Micoulet, A., Dao, M., Lim, C.T., Beil, M. & Seufferlein, T. (2005) Single-cell biomechanics and human disease states: Gastrointestinal cancer and malaria. *Acta Biomaterial.* **1**, 15–30.
- [35] Svitkina, T.M. & Borisy, G.G. (1998) Correlative light and electron microscopy of the cytoskeleton of cultured cells. *Method. Enzymol.* **298**, 570–592.
- [36] Svitkina, T.M. & Borisy, G.G. (1999) Arp2/3 complex and actin depolymerizing factor/cofilin in dendritic organization and treadmilling of actin filament array in lamellipodia. *J. Cell Biol.* **145**, 1009–1026.
- [37] Svitkina, T. (2007) Electron microscopic analysis of the leading edge in migrating cells. *Method. Cell Biol.* **79**, 295–319.
- [38] Walther P. (2008) High-resolution cryo-SEM allows direct identification of F-actin at the inner nuclear membrane of *Xenopus* oocytes by virtue of its structural features. *J. Microsc.* **232(2)**, 379–385.
- [39] Windoffer, R., Wöll, S., Strnad, P. & Leube, R.E. (2004) Identification of novel principles of keratin filament network turnover in living cells. *Mol. Biol. Cell* **15**, 2436–2448.
- [40] Wöll, S., Windoffer, R., Leube, R.E. (2007) p38 MAPK-dependent shaping of the keratin cytoskeleton in cultured cells. *J. Cell Biol.* **177**, 795–807.

A Algorithm for the optimisation of segment positions

The algorithm discussed in this section has been designed to center the line segments of an extracted network graph within the filamentous phase of the binarised tomograms (see Section 3.3). In the following for a voxel $k = (k_1, k_2, k_3) \in \mathbb{N}^3$ the third coordinate will denote height in the image stack and will be referred to as the z-coordinate, whereas k_1 and k_2 are the planar coordinates at 0° -tilt. After binarization by thresholding a tomogram can be viewed as a map $T : V \rightarrow \{0, 1\}$ with bounded discrete domain $V = \{0, \dots, N_1\} \times \{0, \dots, N_2\} \times \{0, \dots, N_3\}$, where the integers N_1, N_2 and $N_3 \in \mathbb{N}$ define the size of the volume. A voxel k such that $T(k) = 1$ will be called a filament voxel, i.e. it is part of the foreground of the binarized tomogram, whereas background voxels have the value $T(k) = 0$. In the following for a given tomogram T we will consider a 3D distance transform $d_T : V \rightarrow \mathbb{Z}$ which is defined as

$$d_T(k) = \begin{cases} \min\{\sqrt{\sum_{i=1}^3 (k_i - m_i)^2} : T(m) = 0\} & \text{if } T(k) = 1, \\ -\min\{\sqrt{\sum_{i=1}^3 (k_i - m_i)^2} : T(m) = 1\} & \text{if } T(k) = 0, \end{cases}$$

i.e., each filament voxel is mapped to its Euclidian distance from the background, whereas each background voxel is mapped to the negative of its distance from the foreground. The 2D analogue of this distance transform is illustrated in Fig. 13.

The position of a line segment S with respect to the foreground, i.e. the filamentous phase, can now be evaluated based on its average length-weighted distance

$$D_T(S) = \frac{1}{|S|} \sum_{k \in V} |Q_k \cap S| d_T(k), \quad (\text{A.1})$$

where $|\cdot|$ is one-dimensional length and

$$Q_k = [k_1 - \frac{1}{2}, k_1 + \frac{1}{2}] \times [k_2 - \frac{1}{2}, k_2 + \frac{1}{2}] \times [k_3 - \frac{1}{2}, k_3 + \frac{1}{2}]$$

denotes the voxel k viewed as a volume element. The illustration for (A.1) in Fig. 13 shows that large values of $D_T(S)$ imply that the segment S is located rather centered within the foreground phase,

whereas small values occur, once S is close to or within the background phase. Notice that $D_T(S)$ can be interpreted as a normalized line integral of the distance transform along S .

In order to optimise the position of the line segments representing the filaments, the algorithm summarized in Fig. 14 was applied. The idea of the optimisation procedure is to randomly shift the positions of vertices. Such a shift is accepted as update of the network graph if the positions of the line segments connected by the vertex have improved in the sense of (A.1). If not, the shift is rejected. The algorithm consists of the following steps:

1. Define a maximum number max of iterations.
2. Select a network vertex at random.
3. Suggest independent and normally distributed shifts with mean 0 and standard deviation $8nm$ in each of the three directions.
4. Evaluate the position of all segments linked by the vertex before and after shifting by (A.1).
5. If the position of all segments linked has improved after shifting, update the network graph by shifting the vertex to the new position.
6. If the number of iterations is less than max , select a new vertex and continue with step 3. With probability 0.9 the new vertex is chosen randomly among the neighbors of the current node, with probability 0.1 it is picked randomly among all vertices.

For our data on average 300 shifts were suggested for each vertex.

As discussed in Section 3.3, a specific flaw in data quality was the inaccurate resolution of the segmented tomograms in z-direction. This resulted from the limited tilt range and a certain oversegmentation in upper network layers, which could not be avoided if threshold values were used which still allowed for identification of lower network components exhibiting decreased contrast. Thus, the segmented tomograms exhibited some filament profiles whose height exceeded their width by up to factor 3. In order to optimally center the line segments in z-direction within the filamentous phase, the above optimization algorithm was also implemented for a modified distance map, defined by

$$\tilde{d}_T(k) = \begin{cases} \min\{|k_3 - m_3| : T(m) = 0\} & \text{if } T(k) = 1, \\ -\min\{|k_3 - m_3| : T(m) = 1\} & \text{if } T(k) = 0. \end{cases}$$

Thus, foreground voxels are mapped to their distance from the background in z-direction and background voxels to the negative of their z-distance to the foreground. This way, certain center voxels of z-stretched oval profiled filaments are mapped to higher values than in case of a regular 3D-distance transform and so the random shift algorithm can be used to center the segments within the oval filament profiles with respect to the z-axis.

Since some filaments presumably not touching each other were stretched in z-direction in the tomograms and thus overlapping, computation of a skeleton resulted in an artificial link between these filaments. In order to remove these artefacts the algorithm monitors all segments shorter than $60nm$ which enclose an angle of no more than 45° with the z-axis. Such a segment is removed if each of the segment ends is integrated into a network vertex of T-shaped topology. This means, that at least two more line segments are emanating from the vertex in a such a way that an angle of more than 90° is enclosed.

The two consecutive steps to improve filament positions based on the two different distance transforms were repeated after each step of graph modification described in Section 3.

B Algorithm for the extrapolation of dead ends

Skeletons computed from binarised tomograms (Fig. 1(b)) frequently exhibit dead ends which are well-known artefacts from skeletonisation and should be removed (Soille, 1999). However, in binarised SEM-tomograms of IF networks some dead ends result from errors in continuity tracking of filaments. In this case they should be extrapolated as shown in Fig. 3 for the IF network data and illustrated

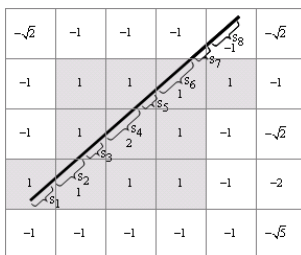


Figure 13: Illustration of the distance transform and the computation of average length-weighted distance for the 2D case. In the setting displayed one obtains $D_T(S) = (s_1 + s_2 + s_3 + 2s_4 + s_6 - s_7 - s_8) / \sum_{j=1}^8 s_j$, where each weight s_j corresponds to one of the intersection lengths $|Q_k \cap S|$ in (A.1).

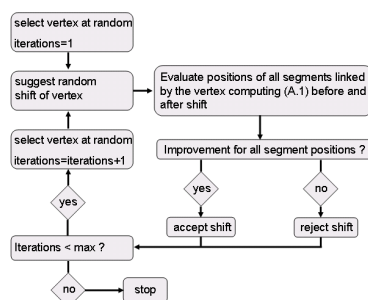


Figure 14: Algorithm for centering the line segments in the filamentous foreground phase.

in Fig. 15. In the following we describe an algorithm constructing extrapolations of dead ends. The algorithm computes possible extrapolations and ranks them according to certain quality criteria. Following the order of this ranking, a plausibility check is performed, investigating whether the trajectory of the extrapolation was affected by shadowing during recording of the SEM tilt series. In this case the extrapolation can be assumed to compensate for a network component which is missing in the segmented 3D image due to its insufficient contrast in the tomogram. The dead end is extrapolated by the highest-ranked connection that passes the plausibility check. If all extrapolations are classified as implausible, the dead end is regarded as a skeletonisation artefact and removed from the network graph. The details discussed in the following are summarized in Fig. 16.

Potential extrapolations considered by the algorithm can be of two different types. If the dead end is extrapolated to another dead end in the network graph an I-connection is established (Fig. 15(a)). Alternatively, the dead end can be extrapolated to a network edge that is integrated into the network with both ends. In this case the algorithm considers the connections to the point on the edge closest to the dead end to be extrapolated. Thus, a T-connection is formed (Fig. 15(b)).

For the potential extrapolations their directional deviation from the orientation of the dead end and their length serve as criteria for a ranking to assess their quality. Directional deviations of more than $\pi/8$ and lengths of more than $0.4\mu\text{m}$ are rejected *a priori*. The remaining extrapolations are then ordered in two different ways, firstly by directional deviation and secondly by their length. In both cases small values are considered as desirable. A total score for an extrapolation is now computed as the weighted mean of these two ranks, where the directional rank is weighted by 0.7 and the distance rank by 0.3. By ordering the potential extrapolations in ascending order of their score, a list is obtained where the quality of extrapolations decreases in list position.

Dead ends which are the result of interrupted filament trajectories due to shadowing effects often possess a dead end counterpart. Thus, I-connections should be regarded as favourable. Therefore, the score-based ranking of the potential extrapolations is modified by moving the I-connections with ranks 1 to 10 to the top of the list (in the internal order of their score-based ranking).

Given the ordered list of potential links it is left to decide whether the extrapolations compensate for shadowing effects in the data or the dead end has to be considered as a skeletonization artefact. For

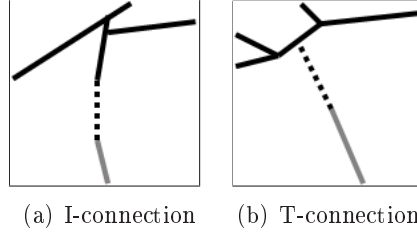


Figure 15: Different extrapolation types. Dead ends are marked in grey, extrapolations are depicted by dotted lines.

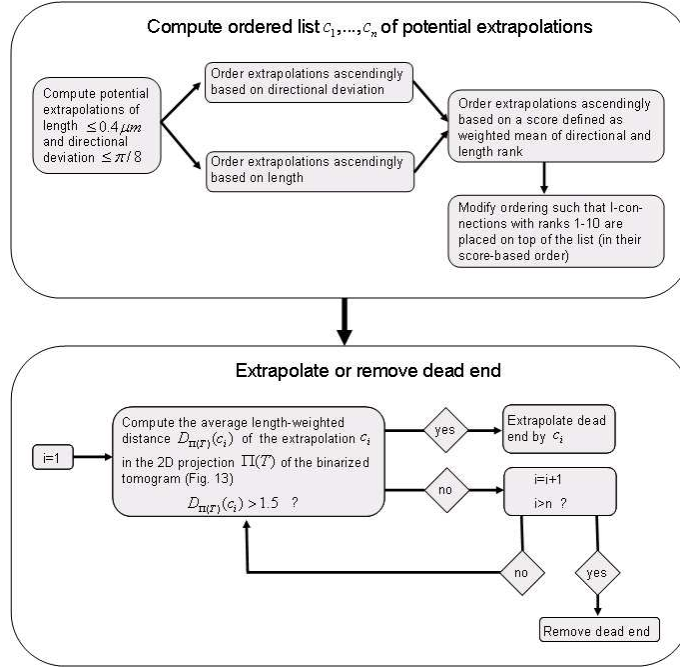


Figure 16: Algorithm for the extrapolation or removal of dead ends.

this purpose a binarized 2D projection $\Pi(T)$ of the 3D tomogram T after thresholding is computed where a pixel (k_1, k_2) is set to 1 whenever there is some $k_3 \in \{0, \dots, N_3\}$ such that $T((k_1, k_2, k_3)) = 1$. Otherwise the pixel is set to 0. Filaments whose projections are covered by $\Pi(T)$ are likely to be affected from shadowing effects. In order to assess the degree of coverage of a potential extrapolation c , its average length-weighted distance $D_{\Pi(T)}(c)$ with respect to $\Pi(T)$ is computed (the principle is illustrated in Fig. 13, the formal definition is analogously to the 3D case discussed in Appendix A). Assuming that all dead ends needing extrapolation are caused by shadowing effects, an extrapolation is accepted once its normalized line integral of the 2D distance transform exceeds 1.5. The dead end is extrapolated by the connection of highest rank that is accepted by this criterion. In case none of the potential extrapolations is accepted, the dead end is considered as an artefact and removed from the network graph unless it is close to the boundary of the observation window.